

Plasmonic V-groove waveguides with Bragg grating filters via nanoimprint lithography

Cameron L. C. Smith,^{1,*} Boris Desiatov,² Ilya Goykmann,² Irene Fernandez-Cuesta,¹ Uriel Levy,² and Anders Kristensen¹

¹Department of Micro- and Nanotechnology, DTU Nanotech, Technical University of Denmark DK-2800 Kongens Lyngby, Denmark

²Department of Applied Physics, The Benin School of Engineering and Computer Science, The Center for Nanoscience and Nanotechnology, The Hebrew University of Jerusalem, Jerusalem 91904, Israel
cameron.smith@nanotech.dtu.dk

Abstract: We demonstrate spectral filtering with state-of-the-art Bragg gratings in plasmonic V-groove waveguides fabricated by wafer scale processing based on nanoimprint lithography. Transmission spectra of the devices having 16 grating periods exhibit spectral rejection of the channel plasmon polaritons with 8.2 dB extinction ratio and -3 dB bandwidth of $\Delta\lambda = 39.9$ nm near telecommunications wavelengths. Near-field scanning optical microscopy measurements verify spectral reflection from the grating structures, and the oscillations of propagating modes along grating-less V-grooves correspond well with effective refractive index values calculated by finite element simulations in COMSOL. The results represent advancement towards the implementation of plasmonic V-grooves with greater functional complexity and mass-production compatibility.

©2012 Optical Society of America

OCIS codes: (230.7380) Waveguides, channeled; (240.6680) Surface plasmons; (350.2770) Gratings.

References and links

1. H. Raether, *Surface Plasmons on Smooth and Rough Surfaces and on Gratings* (Springer-Verlag, Berlin, 1988).
2. W. L. Barnes, A. Dereux, and T. W. Ebbesen, "Surface plasmon subwavelength optics," *Nature* **424**(6950), 824–830 (2003).
3. S. Lal, S. Link, and N. J. Halas, "Nano-optics from sensing to waveguiding," *Nat. Photonics* **1**(11), 641–648 (2007).
4. D. K. Gramotnev and S. I. Bozhevolnyi, "Plasmonics beyond the diffraction limit," *Nat. Photonics* **4**(2), 83–91 (2010).
5. J. R. Krenn, B. Lamprecht, H. Ditlbacher, G. Schider, M. Salerno, A. Leitner, and F. R. Aussenegg, "Non diffraction-limited light transport by gold nanowires," *Europhys. Lett.* **60**(5), 663–669 (2002).
6. R. Zia, J. A. Schuller, and M. L. Brongersma, "Near-field characterization of guided polariton propagation and cutoff in surface plasmon waveguides," *Phys. Rev. B* **74**(16), 165415 (2006).
7. E. Verhagen, A. Polman, and L. K. Kuipers, "Nanofocusing in laterally tapered plasmonic waveguides," *Opt. Express* **16**(1), 45–57 (2008).
8. M. Quinten, A. Leitner, J. R. Krenn, and F. R. Aussenegg, "Electromagnetic energy transport via linear chains of silver nanoparticles," *Opt. Lett.* **23**(17), 1331–1333 (1998).
9. S. A. Maier, P. G. Kik, H. A. Atwater, S. Meltzer, E. Harel, B. E. Koel, and A. A. G. Requicha, "Local detection of electromagnetic energy transport below the diffraction limit in metal nanoparticle plasmon waveguides," *Nat. Mater.* **2**(4), 229–232 (2003).
10. S. Lin, M. Li, E. Dujardin, C. Girard, and S. Mann, "One-dimensional plasmon coupling by facile self-assembly of gold nanoparticles into branched chain networks," *Adv. Mater. (Deerfield Beach Fla.)* **17**(21), 2553–2559 (2005).
11. T. Holmgaard, S. I. Bozhevolnyi, L. Markey, A. Dereux, A. V. Krasavin, P. Bolger, and A. V. Zayats, "Efficient excitation of dielectric-loaded surface plasmon-polariton waveguide modes at telecommunication wavelengths," *Phys. Rev. B* **78**(16), 165431 (2008).
12. J. A. Dionne, L. A. Sweatlock, H. A. Atwater, and A. Polman, "Plasmon slot waveguides: Towards chip-scale propagation with subwavelength-scale localization," *Phys. Rev. B* **73**(3), 035407 (2006).
13. T. W. Ebbesen, C. Genet, and S. I. Bozhevolnyi, "Surface-plasmon circuitry," *Phys. Today* **61**(5), 44–50 (2008).
14. E. N. Economou, "Surface Plasmons in thin films," *Phys. Rev.* **182**(2), 539–554 (1969).

15. I. V. Novikov and A. A. Maradudin, "Channel polaritons," *Phys. Rev. B* **66**(3), 035403 (2002).
16. S. I. Bozhevolnyi, V. S. Volkov, E. Devaux, J. Y. Laluet, and T. W. Ebbesen, "Channelling surface plasmons," *Appl. Phys., A Mater. Sci. Process.* **89**(2), 225–231 (2007).
17. R. F. Oulton, V. J. Sorger, D. A. Genov, D. F. P. Pile, and X. Zhang, "A hybrid plasmonic waveguide for subwavelength confinement and long-range propagation," *Nat. Photonics* **2**(8), 496–500 (2008).
18. I. Goykhman, B. Desiatov, and U. Levy, "Experimental demonstration of locally oxidized hybrid silicon-plasmonic waveguide," *Appl. Phys. Lett.* **97**(14), 141106 (2010).
19. D. Arbel and M. Orenstein, "Plasmonic modes in W-shaped metal-coated silicon grooves," *Opt. Express* **16**(5), 3114–3119 (2008).
20. S. I. Bozhevolnyi, V. S. Volkov, E. Devaux, and T. W. Ebbesen, "Channel plasmon-polariton guiding by subwavelength metal grooves," *Phys. Rev. Lett.* **95**(4), 046802 (2005).
21. S. I. Bozhevolnyi, "Effective-index modeling of channel plasmon polaritons," *Opt. Express* **14**(20), 9467–9476 (2006).
22. D. F. P. Pile and D. K. Gramotnev, "Channel plasmon-polariton in a triangular groove on a metal surface," *Opt. Lett.* **29**(10), 1069–1071 (2004).
23. R. B. Nielsen, I. Fernandez-Cuesta, A. Boltasseva, V. S. Volkov, S. I. Bozhevolnyi, A. Klukowska, and A. Kristensen, "Channel plasmon polariton propagation in nanoimprinted V-groove waveguides," *Opt. Lett.* **33**(23), 2800–2802 (2008).
24. S. I. Bozhevolnyi, V. S. Volkov, E. Devaux, J. Y. Laluet, and T. W. Ebbesen, "Channel plasmon subwavelength waveguide components including interferometers and ring resonators," *Nature* **440**(7083), 508–511 (2006).
25. D. K. Gramotnev and D. F. P. Pile, "Single-mode subwavelength waveguide with channel plasmon-polaritons in triangular grooves on a metal surface," *Appl. Phys. Lett.* **85**(26), 6323–6325 (2004).
26. D. F. Pile and D. K. Gramotnev, "Plasmonic subwavelength waveguides: next to zero losses at sharp bends," *Opt. Lett.* **30**(10), 1186–1188 (2005).
27. V. S. Volkov, S. I. Bozhevolnyi, E. Devaux, J. Y. Laluet, and T. W. Ebbesen, "Wavelength selective nanophotonic components utilizing channel plasmon polaritons," *Nano Lett.* **7**(4), 880–884 (2007).
28. H. Choi, D. F. P. Pile, S. Nam, G. Bartal, and X. Zhang, "Compressing surface plasmons for nano-scale optical focusing," *Opt. Express* **17**(9), 7519–7524 (2009).
29. V. S. Volkov, S. I. Bozhevolnyi, S. G. Rodrigo, L. Martín-Moreno, F. J. García-Vidal, E. Devaux, and T. W. Ebbesen, "Nanofocusing with channel plasmon polaritons," *Nano Lett.* **9**(3), 1278–1282 (2009).
30. S. I. Bozhevolnyi and K. V. Nerkararyan, "Adiabatic nanofocusing of channel plasmon polaritons," *Opt. Lett.* **35**(4), 541–543 (2010).
31. S. I. Bozhevolnyi and K. V. Nerkararyan, "Analytic description of channel plasmon polaritons," *Opt. Lett.* **34**(13), 2039–2041 (2009).
32. V. A. Zenin, V. S. Volkov, Z. Han, S. I. Bozhevolnyi, E. Devaux, and T. W. Ebbesen, "Dispersion of strongly confined channel plasmon polariton modes," *J. Opt. Soc. Am. B* **28**(7), 1596–1602 (2011).
33. E. Moreno, F. J. Garcia-Vidal, S. G. Rodrigo, L. Martin-Moreno, and S. I. Bozhevolnyi, "Channel plasmon-polaritons: modal shape, dispersion, and losses," *Opt. Lett.* **31**(23), 3447–3449 (2006).
34. K. C. Vernon, D. K. Gramotnev, and D. F. P. Pile, "Channel plasmon-polariton modes in V grooves filled with dielectric," *J. Appl. Phys.* **103**(3), 034304 (2008).
35. S. I. Bozhevolnyi and J. Jung, "Scaling for gap plasmon based waveguides," *Opt. Express* **16**(4), 2676–2684 (2008).
36. S. Y. Chou, P. R. Krauss, and P. J. Renstrom, "Imprint of Sub-25 Nm Vias and Trenches in Polymers," *Appl. Phys. Lett.* **67**(21), 3114–3116 (1995).
37. L. J. Guo, "Nanoimprint lithography: Methods and material requirements," *Adv. Mater. (Deerfield Beach Fla.)* **19**(4), 495–513 (2007).
38. I. Fernandez-Cuesta, R. B. Nielsen, A. Boltasseva, X. Borriase, F. Perez-Murano, and A. Kristensen, "V-groove plasmonic waveguides fabricated by nanoimprint lithography," *J. Vac. Sci. Technol. B* **25**(6), 2649–2653 (2007).
39. Commercially available from micro resist technology GmbH, Berlin, Germany, http://www.microresist.de/home_en.htm.
40. S. Jetté-Charbonneau, R. Charbonneau, N. Lahoud, G. Mattiussi, and P. Berini, "Demonstration of Bragg gratings based on long-ranging surface plasmon polariton waveguides," *Opt. Express* **13**(12), 4674–4682 (2005).
41. I. R. Hooper and J. R. Sambles, "Coupled surface plasmon polaritons on thin metal slabs corrugated on both surfaces," *Phys. Rev. B* **70**(4), 045421 (2004).
42. E. D. Palik, *Handbook of Optical Constants of Solids* (Academic, New York, 1985).
43. A. Schleunitz and H. Schiff, "Fabrication of 3D nanoimprint stamps with continuous reliefs using dose-modulated electron beam lithography and thermal reflow," *J. Micromech. Microeng.* **20**(9), 095002 (2010).
44. I. Fernandez-Cuesta, R. B. Nielsen, A. Boltasseva, X. Borriase, F. Perez-Murano, and A. Kristensen, "Excitation of fluorescent nanoparticles by channel plasmon polaritons propagating in V-grooves," *Appl. Phys. Lett.* **95**(20), 203102 (2009).

1. Introduction

Surface plasmon polaritons (SPPs) – electromagnetic waves that propagate along the surface of a metal-dielectric interface [1] – have received renewed interest in recent years due to

technological advances that allow metals to be routinely structured and characterized on the nanoscale. SPPs offer unique attributes to the field of applied optics owing to their ability to concentrate light below the diffraction limit [2–4]. This forms the underlying principle concerning the development of numerous SPP-based subwavelength guiding components such as nanowires [5–7], nanoparticle chains [8–10], dielectric-loaded metal films [11] and plasmonic slot waveguides [12]. The reduced cross section of SPP waveguiding has generated a keen pursuit toward the goal of downscaling photonic circuitry [13], although the simultaneous realization of a configuration with strong confinement and sufficiently low propagation loss has been elusive.

Among the diverse SPP waveguide types available, both subwavelength structures containing dielectric gaps [14] that support *channel* plasmon polaritons (CPPs) [15, 16] and hybrid plasmonic configurations [17, 18] are thought to be most suitable to optimize the trade-off between lateral confinement and propagation loss. In this regard, plasmonic V-shaped (or W-shaped [19]) dielectric gap waveguides are a distinctly promising candidate, where CPP modes are bound to and propagate along the metal groove [20, 21]. V-groove CPP properties offer subwavelength confinement [22], propagation lengths beyond 120 μm for telecommunications wavelengths [23], broadband transmission [24], single moded operation [25] and efficient transmission around sharp bends [26], together enabling the realization of compact Mach-Zender interferometers, Y-splitters, waveguide ring resonators [24], add-drop multiplexers and Bragg grating filters (BGFs) [27]. Furthermore, the intensity distribution of V-groove CPPs are highly tailorable, either by geometrical design for the purposes of nanofocusing [28–30] or confinement optimization [21, 31, 32], or by simply tuning the excitation wavelength [33–35]. Accordingly, V-grooves offer tremendous potential for various near-field-based applications ranging from miniaturized information processing to lab-on-a-chip sensing, although their substantive implementation is dependent on improved device assembly, both in terms of structure quality and fabrication throughput, as well as continued sophistication.

In this work we develop a process for producing plasmonic V-grooves with state-of-the-art BGFs via wafer-scale nanoimprint lithography (NIL) [36, 37]. In contrast to previous work by Volkov *et al.* [27] where a V-groove BGF was created after milling 5 periodic wells across the groove by focused ion beam (FIB), we form the grating corrugation and V-groove profile simultaneously using nanoimprint processes with a pre-defined e-beam lithography (EBL) patterned silicon stamp. Additional fabrication steps subsequently yield devices that are separate and suitable for optical characterization. The technique avoids some of the drawbacks inherent to FIB milling and represents an extension of earlier results that reported on the fabrication of devices containing smooth sidewall V-grooves using NIL technology [23, 38]. To validate the process we experimentally characterize our devices using transmission spectroscopy, showing that a 16-period V-groove BGF exhibits spectral filtering with an 8.2 dB extinction ratio and -3 dB bandwidth of $\Delta\lambda = 39.9$ nm near telecommunications wavelengths. Additionally, we verify the transmission response using near-field scanning optical microscopy (NSOM), showing a distinct wavelength rejection induced by the BGF. The oscillations of the propagating CPP modes observed by the NSOM measurements correspond well with effective refractive index values calculated by finite element simulations in COMSOL. We believe the results denote a key development towards an advanced, mass-production-compatible application of plasmonic V-grooves suitable for purposes ranging from photonic circuit miniaturization to lab-on-a-chip sensing.

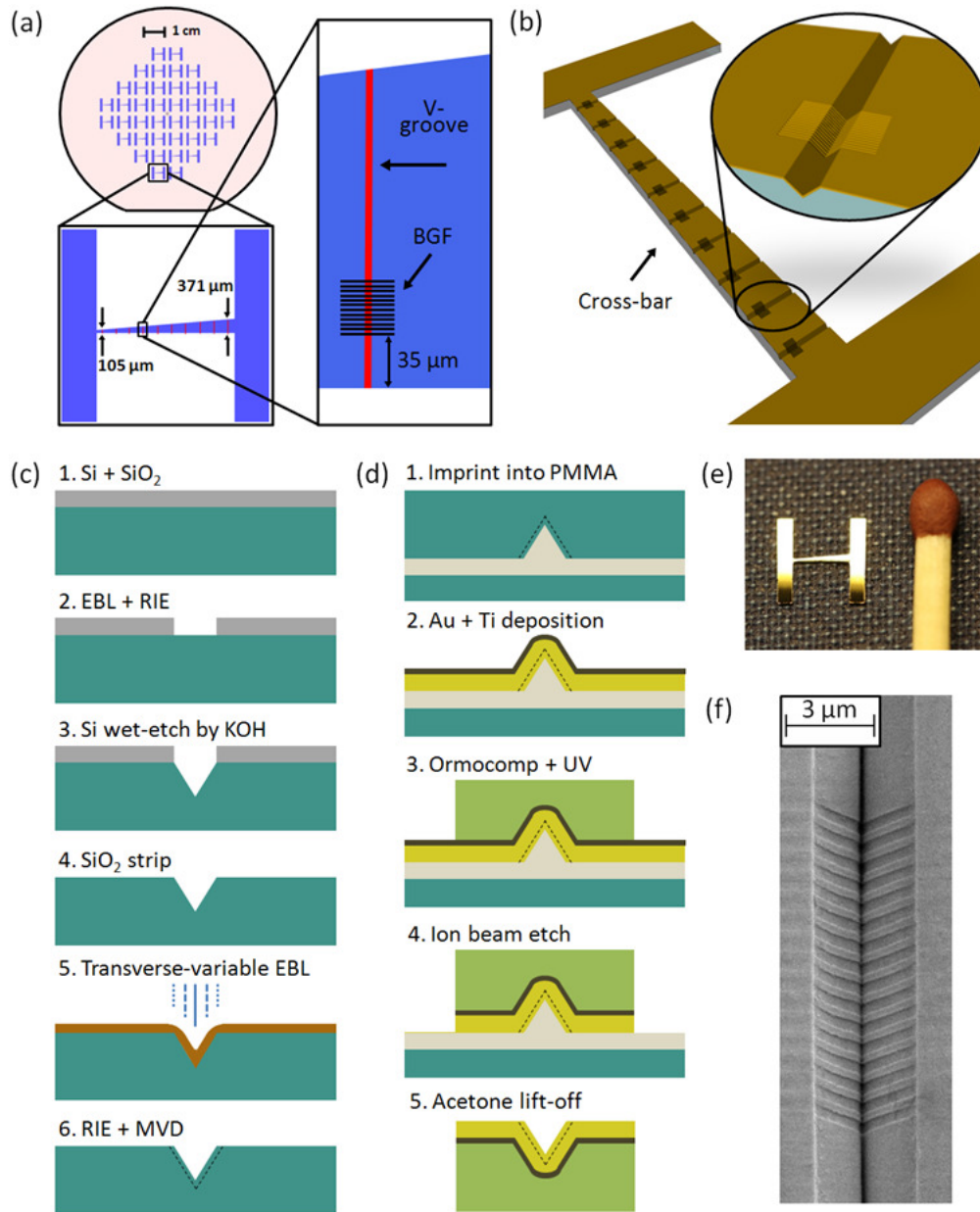


Fig. 1. (a) Distribution of the devices over a 4 inch wafer. (b) Illustration depicting the V-grooves along the device cross-bar. (c) and (d) The fabrication process of both (c) stamp, and (d) device. (e) A 6 mm \times 6 mm gold device next to a common match. The crossbar of the device contains 10 V-grooves. (f) Tilted SEM image of a V-groove containing a BGF.

2. Device and fabrication

The layout of the devices distributed over a 4 inch wafer is shown in Fig. 1(a). Forty devices, each containing 10 V-grooves, are made during a single imprint. The H-like geometry of the devices contains the grooves along the crossbar (Fig. 1(b)), where the crossbar dimensions are chosen to provide a variation in groove length ranging from 105 μm to 371 μm . The V-grooves themselves are designed to be 4.0 μm wide with fixed groove angle 71°, corresponding to a depth of 2.8 μm . The BGFs are located 35 μm away from the flat side end

facet of the V-groove. The overall layout is designed to facilitate end-fire coupling from an optical fiber together with large lapels for ease of handling.

The fabrication of gold V-groove waveguides containing BGFs is illustrated in Figs. 1(c) and 1(d) and is derived from previous works [23, 38]. The process is based on a double replication procedure and consists of stamp fabrication and then device formation in gold on a polymer substrate. The silicon stamp, containing both V-grooves and grating features, is imprinted for the first replication into poly(methylmethacrylate) (PMMA) followed by deposition of a gold layer. A flexible polymer (Ormocomp [39]), cast over the gold and patterned by UV exposure, becomes the device substrate and facilitates the second replication in such a way that the gold maintains the shape, smoothness and vertex sharpness of the initial stamp. The principal advantages of the technique are high quality features, both in terms of the groove sidewalls and the BGF structure, and the ability to perform wafer-scale parallel processing. A resulting device is shown in Fig. 1(e) beside a common match. A scanning electron microscope (SEM) image of a V-groove BGF is shown in Fig. 1(f). More details of the fabrication are described below.

2.1 Stamp fabrication

The stamp fabrication process is illustrated in Fig. 1(b) and is made with a 4 inch (100) silicon wafer. First, a silicon dioxide layer is grown on the silicon substrate and patterned via EBL and reactive ion etching (RIE). The V-grooves are then formed by anisotropic wet etching of the exposed silicon in a KOH bath, where the silicon dioxide openings that allow V-groove formation by the KOH must be parallel to a $\langle 100 \rangle$ crystallographic direction of the substrate. The KOH wet-etch yields smooth V-groove sidewalls with fixed groove angle of 71° . The groove shape may be optionally tailored via an additional oxidation process that reduces (sharpens) the angle [38].

A second EBL step is used to pattern the grating structures. The electron beam dosage is modulated transversally across the V-groove profile such that the groove center is exposed with $200 \mu\text{C}/\text{cm}^2$ and gradually reduced to $100 \mu\text{C}/\text{cm}^2$ at the groove opening ridges. The modulation accounts for the V-groove topography causing a variation of both the EBL resist thickness during spin-coating and the surface distance away from the electron beam focus. The grating structures are then transferred to the silicon substrate by RIE. Finally, after application of an anti-stiction coating by molecular vapor deposition (MVD), the stamp is completed and ready for imprint.

2.2 Device fabrication

Device fabrication by nanoimprint lithography is illustrated in Fig. 1(d). The stamp is imprinted into a $4 \mu\text{m}$ -thick layer of PMMA at 180°C and 15 kN for 30 minutes. An optically thick 200 nm gold layer is evaporated on the PMMA, followed by an additional 10 nm of titanium. A 4 mL volume of Ormocomp is cast over the titanium, maintained at 55°C for 30 minutes to promote adhesion and ensure a uniform $\sim 500 \mu\text{m}$ thick Ormocomp layer. A 100 s UV exposure of the Ormocomp with a UV-mask defines the H-like shape of the substrate for each device and the unexposed material is developed away in Ormodev. The exposed Ormocomp regions are then used as a mask during an ion beam etch to remove the unprotected titanium and gold and assists with obtaining devices with smooth end-facets. The devices are released by dissolving the underlying PMMA layer in an acetone bath with ultrasonic agitation, yielding overall structures shown in Fig. 1(e). The large lapels make for straightforward handling of the single devices, which are individually transferred to an isopropyl alcohol bath for cleaning and finally left to dry. The greater adhesion of titanium to Ormocomp (rather than gold to PMMA) enables the replication of stamp features in gold on Ormocomp. An image of a resulting V-groove containing a 16-period BGF taken by SEM at a 15° tilt is shown in Fig. 1(f).

We measure the BGF dimensions via SEM for both the silicon stamp (Fig. 2(a)) and gold devices (Fig. 2(b)). The periodicity within the stamp is found to be $\Lambda = 761 \pm 10$ nm and in the gold device $\Lambda = 757 \pm 10$ nm, with the uncertainty arising from the SEM resolution. The widths of the V-grooves within the stamp are $4.0 \mu\text{m}$ and in the gold devices $3.4 \mu\text{m}$. This transverse contraction of the device from the stamp may be attributed to Ormocomp shrinkage during the cross-linking step. A reduced magnification SEM image of the BGF and the V-groove is shown in Fig. 2(c). We additionally characterize the fabricated device topography using an atomic force microscope (AFM) (Figs. 2(d) and 2(e)). We show a transverse cross-section of a V-groove in Fig. 2(d), where based on the measurement we estimate the curvature radius of the groove vertex to be 15 nm. A cross-section of the BGF corrugation close to the vertex is shown in Fig. 2(e), where the grating depressions are found to be 96 ± 8 nm deep and the duty cycle averages to 43%.

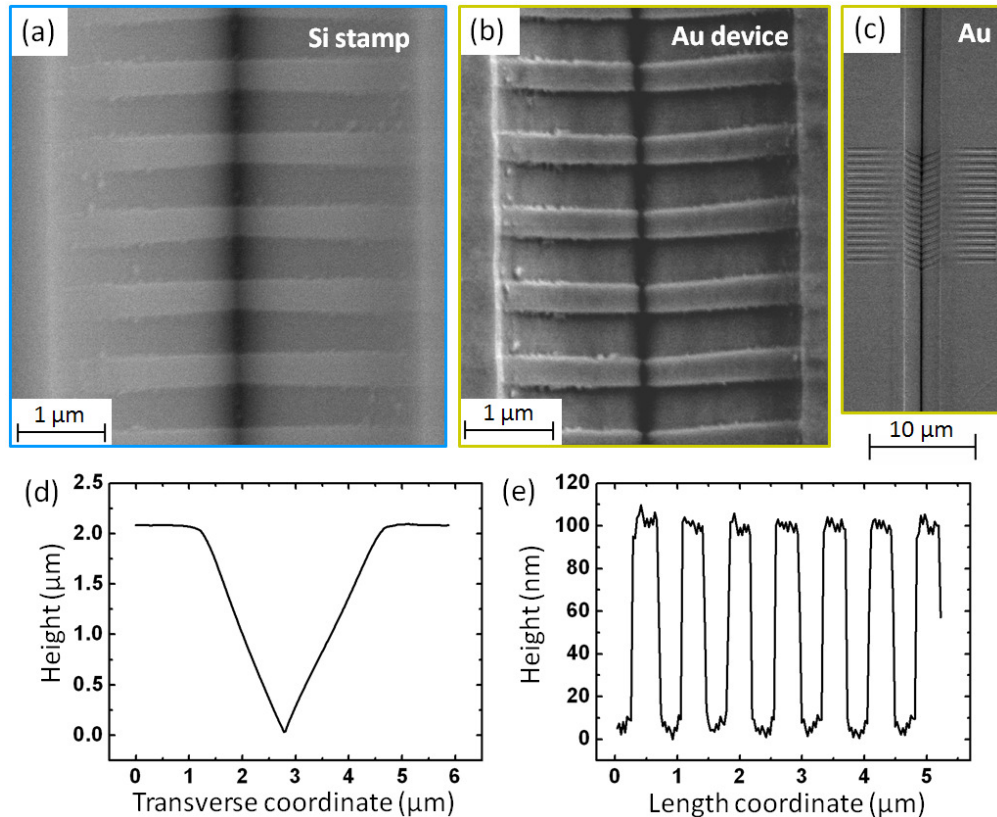


Fig. 2. (a) SEM image of a Si stamp V-groove with BGF. (b) SEM image of a gold V-groove device with BGF. (c) General SEM image showing a V-groove of a gold device with a BGF. (d) Transverse profile of a gold V-groove taken by AFM. (e) BGF topography taken by AFM near a gold V-groove vertex. The corrugation has 96 ± 8 nm depressions with 43% duty cycle.

3. Experimental results

We characterize our devices by NSOM and transmission measurements using similar but separate experimental setups; a schematic is illustrated in Fig. 3. In both cases, two polarization-maintaining (PM) single-moded lensed optical fibers, each placed on 6-axis stages, are used for light launch and collection in an end-fire configuration where the source is transverse-electric polarized (TE-like with the e-field mostly parallel to the device surface plane). A top view far-field microscope objective (visible and IR imaging) is used to assist fiber alignment to the V-grooves. In order to determine exclusive coupling to a CPP mode,

either NSOM scanning or far-field observation of light intensity exiting the V-groove end facet is required.

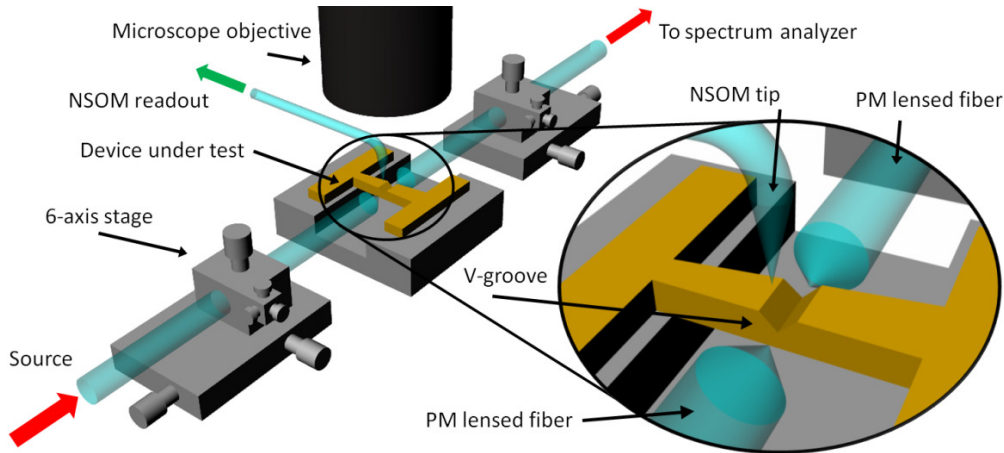


Fig. 3. Experimental setup for NSOM and transmission measurements. Two PM lensed optical fibers on 6-axis stages are used for end-fire launch and collection. A scanning NSOM tip may simultaneously probe the near-field light intensity while light is coupled to the V-groove.

3.1 Transmission spectra

Transmission spectra of the V-groove devices are recorded in a free-space setup as illustrated in Fig. 3 with an optical spectrum analyzer (OSA) (400-1750 nm, Ando AQ-6315E) using a supercontinuum light source (500-1750 nm, SuperK SCB-Compact 100-PC). For launch fiber alignment, an objective is used to focus the output image to an infrared camera that displays the intensity exiting the output V-groove facet and assists with finding the condition for unique CPP coupling (Fig. 4(a)). After alignment is satisfactory, a collection fiber is introduced and positioned, replacing the objective. Due to the straight nature of the waveguides, care is taken to align the collection fiber to reduce the contribution of free space coupling from the launch fiber while maintaining sufficient output signal from the device to overcome the OSA's minimum detection.

The transmission through a 311 μm -length V-groove containing a 16-period (12.1 μm -length) BGF is shown in Fig. 4(b). The spectral signature of the BGF device exhibits a -3 dB bandwidth of $\Delta\lambda = 39.9$ nm with 8.2 dB extinction ratio taken from first reflection minima. This compares to the reported values of: a $\Delta\lambda = 0.5$ nm bandwidth with 10 dB extinction ratio for a 5 mm-length grating in a long-ranging SPP waveguide [40], a reflection coefficient of 25% for 10 air-gap slits (4 μm -length) on a metal ridge SPP waveguide [41], and a factor of ~ 3 suppression over a bandwidth of $\Delta\lambda = \sim 100$ nm for a 5-period (3.75 μm -length) grating in a FIB milled V-groove CPP waveguide [27]. In the inset in Fig. 4(b), the reference transmission through a similar but grating-less V-groove (no BGF) in dBm scale is shown. As can be expected, longer wavelengths propagate further along the V-groove – i.e. lower propagation loss – due to decreasing confinement to the metal.

We apply a Gaussian fit to the bandstop region for the BGF trace in Fig. 4(b) to assist determining the transmission minimum, found to occur at a free-space wavelength of $\lambda_0 = 1454$ nm. This value is close to twice the BGF period but 4% shorter. When applying a periodic stacked media approach we are unable to accurately reconcile the spectral position of the measured peak reflection and therefore at present do not offer a rigorous explanation for the offset. However, a similar result has been observed by Volkov *et al.* [27], where the possible involvement of more complicated physical phenomena is mentioned. The difference in extent of the wavelength offset from two times the BGF period (4% in our case versus 2% in [27]) suggests that the variation in geometrical parameters such as V-groove angle and the

BGF corrugation profile play a role. Nevertheless, we refrain from definitive conclusions until further detailed investigations are made.

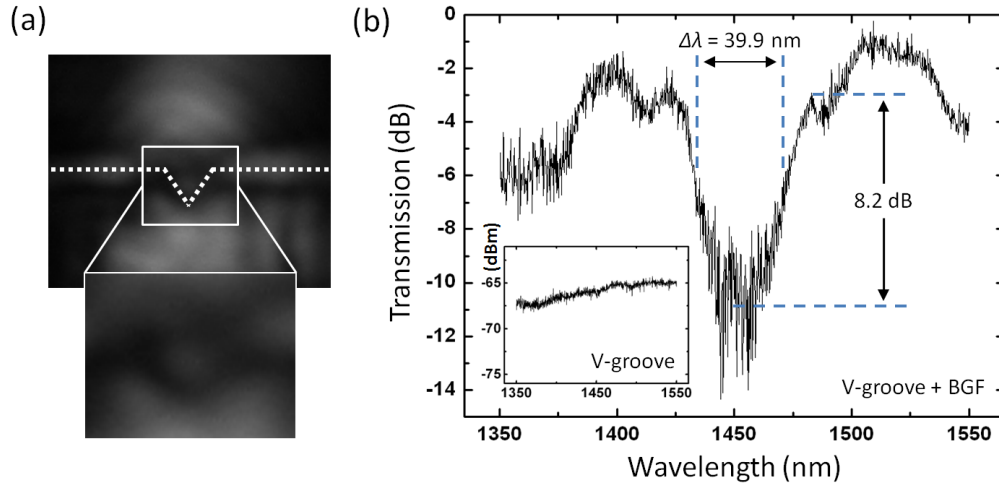


Fig. 4. Transmission measurements. (a) Light intensity exiting a V-groove end facet imaged with an objective and IR camera, showing successful coupling to a CPP mode. (b) Transmission spectrum through a 311 μm -length V-groove containing a BGF using a PM lensed fiber for collection. The filter -3 dB bandwidth is $\Delta\lambda = 39.9$ nm and the extinction ratio is 8.2 dB. The center wavelength is $\lambda = 1454.4$ nm. Inset: reference transmission (vertical axis is dBm units) obtained for a similar V-groove without BGF.

3.2 Near-field scanning optical spectroscopy measurements

In Fig. 5 we verify the transmission results via NSOM scanning measurements performed on plain and BGF-containing V-grooves using a free-space experimental setup as illustrated in Fig. 3. The NSOM tip is metallic coated with 300 nm aperture (NANONICS MultiView 4000), a tunable laser source (1460-1580 nm, Agilent 81680A) is used to excite the CPPs and a pW InGaAs Agilent 81634B detector assists with alignment. The CPP mode, propagating left to right, is represented in the figures by the local intensity collected along the scanning path of the NSOM tip. It is important to remark that the intensity is collected only where the NSOM tip's shape and size are permitted within the transverse V-groove profile [32].

NSOM measurements along a 311 μm -length V-groove containing a 16-period BGF are presented in Figs. 5(a), 5(b) and 5(c), displaying the response both within the Bragg reflection band, $\lambda = 1465$ nm, and beyond, $\lambda = 1550$ nm. Both images are obtained with the same fiber coupling arrangement. The scanning field regions in Figs. 5(b) and 5(c) are $5.0 \mu\text{m} \times 27.9 \mu\text{m}$, where the observed curvature of the CPP propagation is attributed to drifts during measurement. It is clear that rejection of the propagating light occurs for $\lambda = 1465$ nm as it interacts with the grating corrugation, while for $\lambda = 1550$ nm this effect is reduced. The topography obtained by an AFM scan along the V-groove is shown in Fig. 5(d) with a cross-section close to the vertex plotted in Fig. 5(e).

To provide a reference for the above measurements, we perform NSOM scans along a similar but grating-less V-groove, shown in Figs. 5(f), 5(g) and 5(h), again for the excitation wavelengths of $\lambda = 1465$ nm and $\lambda = 1550$ nm. The panel region is $5.0 \mu\text{m} \times 15.0 \mu\text{m}$ to reduce defects and drift. The topography obtained by AFM scan along the V-groove section is plotted in Figs. 5(i) and 5(j).

We obtain the propagation lengths for the CPPs from an exponential fit of the optical signal along the propagation direction. These are found to be $\alpha^{-1} = 30.3 \mu\text{m}$ and $\alpha^{-1} = 36.0 \mu\text{m}$ for the excitation wavelengths $\lambda = 1465$ nm and $\lambda = 1550$ nm respectively. As noted in other work previously [23], there is a non-negligible dependence on the coupling arrangement in

terms of the angular alignment of the launch fiber and the profile of the V-groove end-facet. Nevertheless, these values are in agreement with relative propagation lengths excited by the different wavelengths [23].

The extinction ratio offered by the BGF in Fig. 5(b), I_o/I_i , is found to be 4.5 ± 0.9 , where I_i and I_o are taken before and after the corrugation at $8 \mu\text{m}$ and $23 \mu\text{m}$ propagation coordinates respectively. The uncertainty is related to measurement noise and the propagation loss determined from Fig. 5(g) is considered. Although the signal to noise ratio is low, it is nevertheless clear that the optical signal reduces rapidly within the BGF region, indicating that a smaller number of periods would suffice to provide reasonable wavelength rejection.

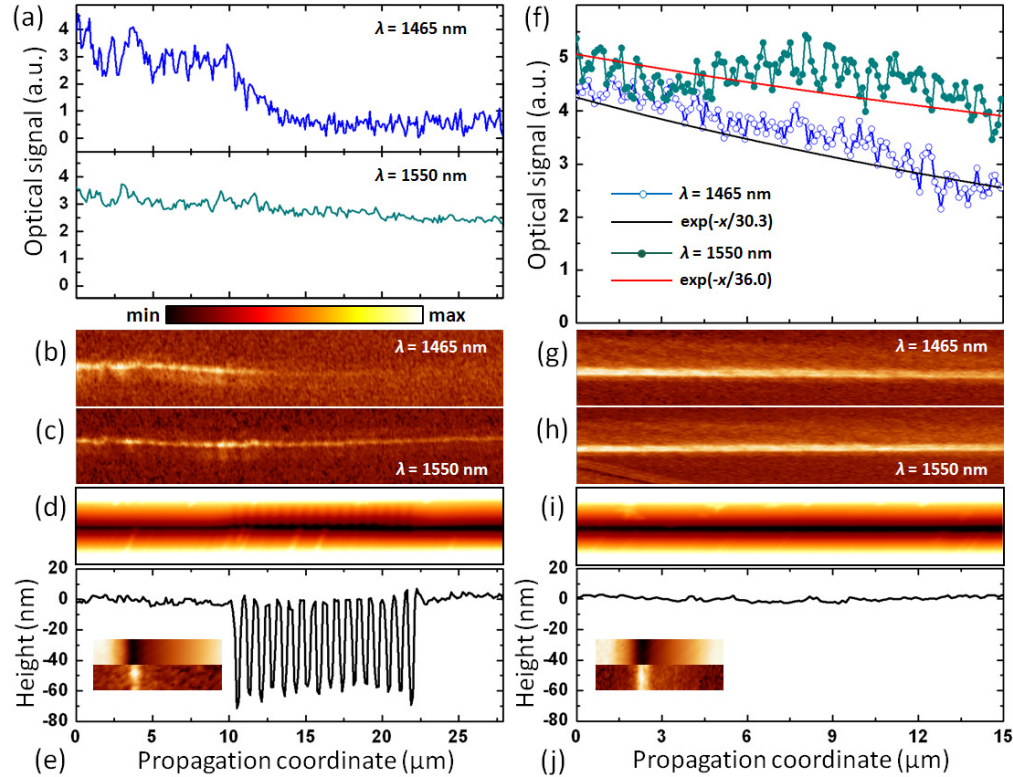


Fig. 5. (a), (b) and (c): NSOM measurements for a V-groove containing a 16-period BGF. (a) Intensity profiles along the V-groove taken from the $5.0 \times 27.9 \mu\text{m}$ panels of (b) and (c) for the excitation wavelengths $\lambda = 1465 \text{ nm}$ and $\lambda = 1550 \text{ nm}$ respectively. (d) Topographical image taken by AFM for the same region of (b) and (c). (e) Cross-section close to the V-groove vertex from (d) with inset: $5 \times 1 \mu\text{m}$ panels showing topography and near field optical intensity ($\lambda = 1550 \text{ nm}$) taken simultaneously by NSOM probe. (f), (g) and (h): NSOM measurements for a V-groove without BGF. (f) Intensity profiles with fitted propagation decay curves along the V-groove taken from the $5.0 \times 15.0 \mu\text{m}$ panels (g) and (h) for the excitation wavelengths $\lambda = 1465 \text{ nm}$ and $\lambda = 1550 \text{ nm}$ respectively. (i) Topographical image taken by AFM for the same region of (g) and (h). (j) Cross-section close to the V-groove vertex from (i) with inset: $5 \times 1 \mu\text{m}$ panels showing topography and near field intensity ($\lambda = 1550 \text{ nm}$) taken simultaneously by NSOM probe.

4. Simulation and comparison with experiment

We perform finite element method (FEM) simulations in COMSOL for $3.4 \mu\text{m}$ -wide gold V-grooves similar to fabricated devices, shown in Figs. 6(a) and 6(b) as time-averaged intensity distributions for the optical modes of $\lambda = 1465 \text{ nm}$ and $\lambda = 1550 \text{ nm}$. We consider only TE polarized incident light where the E-field is oriented parallel with the horizontal surface plane and use tabular gold dielectric constants [42]. We have filleted the V-groove corner features

to 15 nm curvature radius at the vertices and wedges in order for the simulated structures to correspond with real devices and avoid computational singularities.

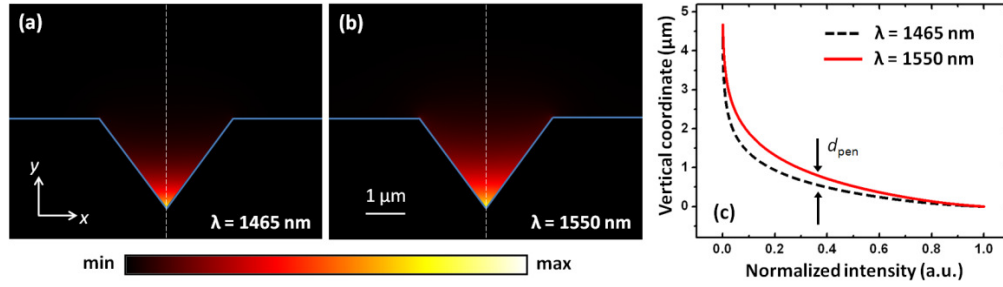


Fig. 6. Intensity distributions of the fundamental optical modes for a 3.4 μm -wide gold V-groove excited by free-space wavelengths (a) $\lambda = 1465$ nm and (b) $\lambda = 1550$ nm. Panels are 6×8 μm . (c) Vertical intensity profiles obtained in (a) (dashed black) and (b) (solid red) taken along the y coordinate at the V-groove vertices.

The effective refractive indices of the calculated CPP modes are found to be $n_{\text{eff}}(1465 \text{ nm}) = 1.016 + i1.860 \times 10^{-3}$ and $n_{\text{eff}}(1550 \text{ nm}) = 1.010 + i9.948 \times 10^{-4}$. We compare these values with the near-field oscillations of the propagating CPPs obtained via NSOM measurements in Figs. 5(g) and 5(h). The CPP intensity oscillation excited by a coherent source should follow $\lambda/2n_{\text{eff}}$ – i.e. $\lambda = 1465 \text{ nm} \rightarrow 721.0 \text{ nm}$ and $\lambda = 1550 \text{ nm} \rightarrow 767.3 \text{ nm}$. Applying a Gaussian fit to the periodic peaks found in Figs. 5(g) and 5(h), we arrive at average oscillations of 715 nm and 765 nm, respectively, indicating that the experimental oscillations are in agreement with prediction and lie within ± 10 nm of data resolution uncertainty. A summary of the values obtained from FEM calculations and experiments are represented in Table 1.

Table 1. Numerically Calculated and Experimental CPP Mode Characteristics

$\lambda_{\text{free space}}$	$n_{\text{eff}}(\text{FEM})$	$\lambda_{\text{CPP}}/2(\text{FEM})$	$\lambda_{\text{CPP}}/2(\text{exp})$	$d_{\text{pen}}(\text{FEM})$	$\alpha^{-1}(\text{FEM})$	$\alpha^{-1}(\text{exp})$
1465 nm	$1.016 + i1.860 \times 10^{-3}$	721.0 nm	715 nm \pm 10 nm	538.5 nm	62.7 nm	30.3 nm
1550 nm	$1.010 + i9.948 \times 10^{-4}$	767.3 nm	765 nm \pm 10 nm	789.8 nm	124.0 nm	36.0 nm

CPPs excited by longer free space wavelengths exhibit increasing extensions of the propagating mode intensity away from the V-groove metal surface, as shown in Fig. 6(c). In our case, a 5.8% wavelength increase ($\lambda = 1465 \text{ nm} \rightarrow 1550 \text{ nm}$) corresponds to a 46.7% increase in penetration of the mode profile into the air ($d_{\text{pen}} = 538.5 \text{ nm} \rightarrow 789.8 \text{ nm}$), taken as the $1/e$ intensity decay vertically upward from the V-groove vertex. This relates to the reduced propagation loss of longer wavelength CPPs since proportionally more energy of the mode is in air rather than the lossy metal. From the imaginary part of the refractive index we calculate the propagation lengths to be $\alpha^{-1} = 62.7 \mu\text{m}$ and $\alpha^{-1} = 124.0 \mu\text{m}$ for the wavelengths $\lambda = 1465$ nm and $\lambda = 1550$ nm, respectively. The lower measured values of propagation lengths may be attributed to imperfection in the V-groove shape, metal roughness, water condensation and inferior properties of the thin metallic layer as compared with bulk properties.

5. Conclusion

We report on the demonstration of wavelength filtering via Bragg gratings in gold V-groove waveguides fabricated by wafer-scale nanoimprint lithography. We optically characterize fabricated devices using both transmission and NSOM measurements near telecommunications wavelengths. We show that 16 grating periods exhibit an 8.2 dB extinction ratio of the CPPs at the rejection wavelength with a -3 dB bandwidth of $\Delta\lambda = 39.9$

nm. A 4% shortening of the central rejection wavelength from twice the BGF period could not be explained solely by device shrinkage and Bragg stack calculations, and a comparison with other similar work suggests that geometrical parameters such as V-groove angle and BGF corrugation profile play a deeper role. NSOM measurements verify spectral filtering from the grating structures, and the oscillations of propagating CPP modes along grating-less V-grooves are in agreement with effective refractive index values calculated by finite element simulations in COMSOL.

We remark that, in addition to the high quality features and the ability to characterize device transmission properties, the fabrication process to form BGFs in plasmonic V-grooves can be readily translated to operate at visible wavelengths for both shallower and deeper V-groove geometries. Furthermore, it is reasonable to consider implementing a second order surface grating coupler to facilitate improved coupling to the V-groove CPPs, thus avoiding the momentum mismatch issues that are inherent to the end-fire coupling technique while also mitigating the problem of fiber coupling dependence. As of this writing, however, the approach suffers one important drawback compared to its FIB milling counterpart: it cannot produce curved waveguides owing to the crystallographic-based wet-etch step in the stamp production. While the resulting sidewalls are smooth, the potential for immediate application is currently limited. Nevertheless, recently developed processes offer promise in this regard, such as variable e-beam exposures to define the waveguides [43] and a following oxidation step to controllably sharpen the V-groove vertices [38].

Finally, we believe the findings represent an important milestone towards a sophisticated, mass-production-compatible application of plasmonic V-grooves for not only photonic circuit miniaturization but also lab-on-a-chip sensing. For example, the micron and sub-micron V-groove profiles mark a physically clear and addressable location of interest, e.g. for surface functionalization or the development of fluorescent point sources [44], and are also highly suitable to simultaneously act as micro or nanofluidic channels. The prospects of plasmonic V-grooves within the context of a lab-on-a-chip platform are made particularly promising due to the widely tunable intensity distribution of the propagating CPP evanescent field, for purposes such as 3-dimensional optical scanning or field overlap control.

Acknowledgments

Cameron L. C. Smith is supported by an EU FP7 Marie Curie Fellowship (project number PIIIF-GA-2009-254573). Ilya Goykhman and Boris Desiatov acknowledge the Eshkol fellowship awarded by the Israeli ministry of science. Irene Fernandez-Cuesta is supported by an EU FP7 Marie Curie Fellowship (project number PEOF-GA-2009-254498). The authors gratefully acknowledge funding from the EC-funded project NaPANIL under grant agreement no. 214249. The authors thank the Metamaterials Group from DTU Fotonik for providing the experimental setup to measure the transmission properties of the V-grooves.